Received: 22 April 2024 | Revised: 12 June 2024 | Accepted: 22 June 2024

DOI: 10.1111/jace.20031

RESEARCH ARTICLE

Journal of the American Ceramic Society

Phase transition in $Eu_2Zr_{2-x}O_{7-2x}$ ($x = 0$–1) solid solutions: A combined structural and spectroscopic study

Linggen Kong | **Zhiyang Wang** | **Inna Karatchevtseva** | **Yingjie Zhang**

Australian Nuclear Science and Technology Organisation, Kirrawee DC, New South Wales, Australia

Correspondence
Linggen Kong and Yingjie Zhang, Australian Nuclear Science and Technology Organisation, Locked Bag 2001, Kirrawee DC, NSW 2232, Australia.
Email: lnk@ansto.gov.au and yzx@ansto.gov.au

Zirconate pyrochlores have been extensively studied as candidate waste forms for the immobilization of actinide wastes due to their flexible crystal chemistry, excellent structural stability, and exceptional radiation tolerance. Herein, we report the synthesis of a series of compounds $Eu_2Zr_{2-x}O_{7-2x}$ ($x = 0$–1, step = 0.125) using a co-precipitation route to form solid solutions between the two end members, $Eu_2Zr_2O_7$ pyrochlore and Eu_2ZrO_5 defect fluorite. It is important to understand the pyrochlore to defect fluorite transformation as a function of Zr/Ln molar ratio. The structural investigation by x-ray diffraction has shown the increasing cation disorder and corresponding structural transitions from the ordered pyrochlore to disordered pyrochlore, then to defect fluorite. While diffuse reflectance spectroscopy provides similar optical absorption features reflecting the presence of Eu(III) ion, Raman spectroscopy has revealed more details on the phase transition and short-range structures. This work highlights the structural flexibility in zirconate materials as potential nuclear waste forms for the immobilization of actinide-rich waste streams, especially suitable for the separated minor actinides.

KEYWORDS
europium zirconate, fluorite, order to disorder, phase transition, pyrochlore

1 | INTRODUCTION

The resurgent interest in nuclear energy has led to a growing investment in the current uranium-based nuclear fuel cycle (NFC).[1–3] Of particular interest is the safe treatment and disposal of high-level wastes (HLWs) either as the spent nuclear fuel (SNF) discharged from the nuclear reactors or the chemical reprocessing of SNF.[4,5] As candidate waste forms for HLWs, various chemically durable mineral phases such as zirconolite,[6–8] pyrochlore,[9–11] brannerite,[12–14] and phosphates[15–17] have been extensively studied. In addition, advanced glass–ceramic composite waste forms based on these ceramic phases have also been developed.[18–25]

Due to the remarkable properties such as excellent radiation tolerance, high chemical durability, and ability to incorporate a range of actinides into the structures, lanthanide zirconate oxides with either a pyrochlore or fluorite structure[26] have gained great interest in various applications including nuclear waste forms.[27–36] Within the derivatives of the prototype fluorite structure (AO_2, space group $Fm\bar{3}m$), the most often studied lanthanide zirconates include ordered pyrochlore $Ln_2Zr_2O_7$ ($Ln =$ lanthanides) (space group $Fd\bar{3}m$),[37–41] and the defect fluorite Ln_2ZrO_5 (space group $Fm\bar{3}m$).[42–49] An oxide pyrochlore review[50] derives an empirically stability field for stable pyrochlore formation $A_2B_2O_7$ within the cation ionic radii ratios (r_A/r_B) between 1.46 and 1.80. Hence, $Ln_2Zr_2O_7$ ($Ln =$ La–Gd) compounds are expected to form pyrochlore structure, while zirconates with lanthanides smaller than Gd tend to form fluorite structure. On the other hand, systematic studies on stoichiometric Ln_2ZrO_5 zirconates[51,52] show the complexity of the crystal structures for several compounds (Ln = Sm, Gd, Tb, Dy). These structures tend to present as either fluorite-like or pyrochlore-like with diffuse features found within the electron diffraction patterns showing the presence of modulated structure. A recent study[42] produced single-phase Ln_2ZrO_5 (Ln = Sm, Eu, Gd, Tb) compounds at 1400°C. The crystal structures are investigated by neutron/synchrotron x-ray powder diffraction, with the defect-fluorite type structure, with $Fm\bar{3}m$ symmetry being confirmed by the general long-range structure investigation. In addition, the Eu-Zr-O phase diagram[53,54] predicts small regions of single phase at both end members, pyrochlore at $Eu_2Zr_2O_7$ and fluorite at Eu_2ZrO_5, while the solid solutions contain both pyrochlore and fluorite phases in the middle region, at elevated temperatures.

From synthesis point of view, relatively low temperature is required to form titanate compounds compared with the zirconates. However, the titanate pyrochlore is usually susceptible to radiation damage when it is utilized for nuclear-related applications.[55] Even though Ln_2TiO_5 titanate having smaller radii shows better radiation tolerance, compared with $Ln_2Ti_2O_7$,[56] it usually requires relatively higher sintering temperatures.[57,58]

Zirconates normally exhibit high resistance to radiation damage; however, they usually need more energy to produce compared with the titanate counterparts. Fortunately, the wet-chemistry method ensures the mixing of precursors at the molecular level, thus promotes the reactivity of the reactants, and enhances the homogeneity of the products. In addition, some Ln_2O_3–ZrO_2 systems may contain compounds that undergo phase transitions from ordered pyrochlore $Ln_2Zr_2O_7$ to defect fluorite Ln_2ZrO_5 (Ln = Pm, Sm, Eu),[51,52] thus they are the subject of the research for specific applications, for example, ionic conductors.[48,59,60] As a result, it is important to understand the pyrochlore to defect fluorite phase transition relating to not only the composition changes but also the Zr/Ln molar ratio.

In this study, the $Eu_2Zr_{2-x}O_{7-2x}$ (x = 0–1, step = 0.125) solid solutions were synthesized using a co-precipitation method, followed by sintering at 1400°C in air. The materials were then characterized using powder x-ray diffraction, diffuse reflectance, and Raman spectroscopies to probe the average and local structures, and the phase transition from ordered pyrochlore to defect fluorite as the Zr/Eu molar ratio decreases from 1 to 0.5. The gradual phase transitions showed the flexible crystal chemistry of zirconates, enabling them good candidate waste forms for HLWs arising from the NFC.

2 | EXPERIMENTAL

2.1 | Materials fabrication

Analytical reagent grade europium(III) nitrate hydrate [$Eu(NO_3)_3{\cdot}xH_2O$] (≥99.9%) and zirconyl nitrate hydrate [$ZrO(NO_3)_2{\cdot}xH_2O$] (≥99%) were used as received from Sigma-Aldrich (Merck), with the metal content quantitatively determined by gravimetric analyses. Milli-Q grade water was used in all the experiments.

The calculated amounts of europium nitrate and zirconyl nitrate were dissolved in 100 mL of water, followed by adding an ammonia solution (1.7 mol/L) dropwise under stirring until pH = ~11. The resultant precipitate was stirred for 1 h and separated by centrifugation, dried at 100°C, and then calcined for 4 h at 750°C in air with a ramp rate of 2°C/min. The calcined powder was pelletized and sintered for 24 h at 1400°C in air with 5°C/min heating/cooling rate. Sample details are summarized in Table 1.

2.2 | Materials characterization

Powder x-ray diffraction (PXRD) patterns were acquired using a Bruker D8 x-ray diffractometer equipped with Cu K_α (λ = 1.5418 Å) radiation in the 2θ range of 5°–80° with 2θ step size of 0.02° and an acquisition time of 2 s

TABLE 1 Samples with different compositions and mol% for each binary oxide.

$Eu_2Zr_{2-x}O_{7-2x}$	Composition	$EuO_{1.5}/ZrO_2$ (mol%)	Eu_2O_3/ZrO_2 (mol%)
$x = 0$	$Eu_2Zr_2O_7$	50.0/50.0	33.3/66.7
$x = 0.125$	$Eu_2Zr_{1.875}O_{6.75}$	51.6/48.4	34.8/65.2
$x = 0.25$	$Eu_2Zr_{1.75}\ O_{6.5}$	53.3/46.7	36.4/63.6
$x = 0.375$	$Eu_2Zr_{1.625}O_{6.25}$	55.2/44.8	38.1/61.9
$x = 0.5$	$Eu_2Zr_{1.5}O_6$	57.1/42.9	40.0/60.0
$x = 0.625$	$Eu_2Zr_{1.375}\ O_{5.75}$	59.3/40.7	42.1/57.9
$x = 0.75$	$Eu_2Zr_{1.25}O_{5.5}$	61.5/38.5	44.4/55.6
$x = 0.875$	$Eu_2Zr_{1.125}O_{5.25}$	64.0/36.0	47.1/52.9
$x = 1.0$	Eu_2ZrO_5	66.7/33.3	50.0/50.0

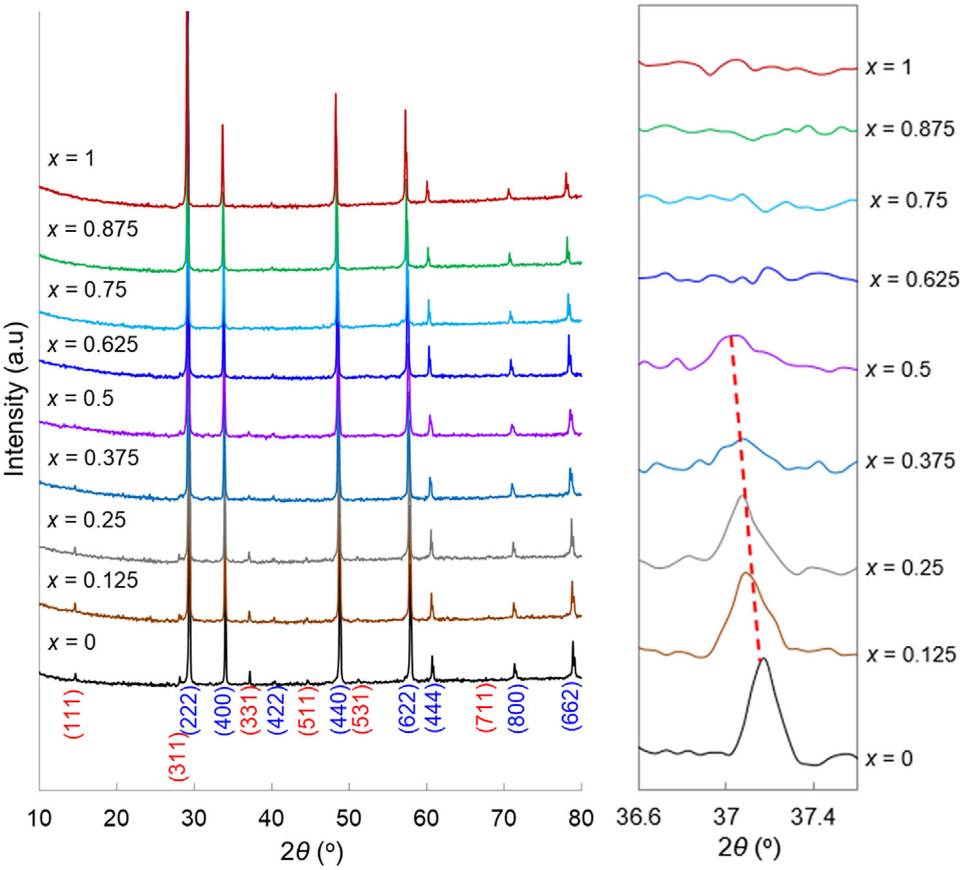

FIGURE 1 PXRD patterns of the $Eu_2Zr_{2-x}O_{7-2x}$ ($x = 0$–1) solid solutions showing the phase transition from $Eu_2Zr_2O_7$ ordered pyrochlore to disordered pyrochlores ($x = 0.125$–0.5), then to defect fluorites ($x = 0.625$–1). Pyrochlore (hkl) reflections are labeled in blue and red with superlattice reflections highlighted in red. Diffraction data in the 2θ range of approximately 36.6°–37.6° are shown on the right to highlight the evolution of (331) superlattice reflection for the pyrochlores.

per step. The PXRD data were analyzed using the Rietveld structure refinement method with the TOPAS (version 5) program.[61] The diffraction peak profile was modeled using a pseudo-Voigt function, and the diffraction background was fit with an eighth order Chebyschev polynomial function. The existing $Fd\bar{3}m$ structural model for the pyrochlore[62] and the $Fm\bar{3}m$ model for defect fluorite structure[63] have been referenced in the Rietveld refinements. The zero-point error, unit cell parameters, isotropic temperature factor, the only variable atomic position parameter (O 48*f* *x*-coordinate, for all the pyrochlores) and the mixed occupancy of Eu/Zr cation sites (16*c* and 16*d*), for disordered pyrochlore compositions ($x = 0.125$ and 0.25) were refined. The O anion sites 48*f* and 8*b* for all the pyrochlores and the mixed site occupancy parameters for Zr cations, as well as some highly disordered pyrochlores ($x = 0.375$ and 0.5) are constrained to be equally occupied based on their stoichiometries and the identified order/disorder nature.

Diffuse reflectance spectra (DRS) were measured in the UV–vis and NIR regions on an Agilent Cary 5000 spectrophotometer with a Labsphere Biconical Accessory. Raman spectra were collected using a Renishaw inVia Raman spectrometer equipped with the excitation Argon ion laser 532 and 785 nm, and a Peltier cooled charge-coupled device (CCD) detector (Renishaw plc) at room temperature. Stokes shifted Raman spectra were collected in the static mode in the range of approximately 100–1000 cm^{-1} with a spectral resolution of approximately 1.7 cm^{-1} for the 1800 L/mm grating. The spot size was around 1.5 μm for 50× magnification.

3 | RESULTS AND DISCUSSION

3.1 | Crystal structures and phase transition

Figure 1 shows the PXRD patterns of the $Eu_2Zr_{2-x}O_{7-2x}$ ($x = 0$–1) solid solutions. The end member $Eu_2Zr_2O_7$ ($x = 0$) composition shows an ordered pyrochlore structure (space group $Fd\bar{3}m$, indexed based on ICSD 130791), as evidenced by a few superlattice reflections including (111), (311), (331) and (511), and so forth, in addition to the principal reflections such as (222), (400), (440), and (622), and so forth. Diffraction data in the 2θ range of approximately 36.6°–37.6° with the relatively strong superlattice reflection (331) for the pyrochlore structure are highlighted in Figure 1 to show the subtle structural transition along the series. The intensities of the (331) superlattice reflection appear to gradually decrease with increasing x from 0 ($Eu_2Zr_2O_7$) to 0.5 ($Eu_2Zr_{1.5}O_6$), then disappear at $x \geq 0.625$. These observations suggest the phase transition occurs in the $Eu_2Zr_{2-x}O_{7-2x}$ system from the $Eu_2Zr_2O_7$ ordered pyrochlore, to the disordered pyrochlores ($x = 0.125$–0.5), then to defect fluorites ($x = 0.625$–1). Rietveld refinements of PXRD data are further performed to confirm these phase transitions.

Figure 2 presents the Rietveld refinements for three typical compositions within $Eu_2Zr_{2-x}O_{7-2x}$ solid solutions including $Eu_2Zr_2O_7$ ($x = 0$) with ordered pyrochlore structure, $Eu_2Zr_{1.5}O_6$ ($x = 0.5$) with disordered pyrochlore structure, and defect fluorite Eu_2ZrO_5 ($x = 1$). The detailed refinement results are summarized in Table 2. As shown in Figure 2A, the ordered pyrochlore structure model fits the $Eu_2Zr_2O_7$ experimental PXRD pattern well ($R_{wp} = 0.023$, $R_{wp} = 0.015$, and $R_p = 0.016$), including the weak superlattice reflections such as (111) and (331). This result confirms the highly ordered nature of the investigated $Eu_2Zr_2O_7$ composition. As represented by the $Eu_2Zr_{1.5}O_6$ refinement for the disordered pyrochlore structure (Figure 2B) and by the Eu_2ZrO_5 result for the defect fluorite structure (Figure 2C), all the other refinements converge with good fitting qualities (Table 2). Note that the disordering in the $Eu_2Zr_{2-x}O_{7-2x}$ pyrochlore compositions ($x = 0.125$–0.5) is structurally described by the mixed site occupancies for the Eu/Zr cation sites (16d and 16c). Such disordered pyrochlore structure model used in the refinements reasonably predicts the weak superlattice reflections, as typically shown in Figure 2B. To confirm the disordering nature in the $Eu_2Zr_{2-x}O_{7-2x}$ pyrochlore compositions ($x = 0.125$–0.5), we also attempt to model the PXRD data using the ordered pyrochlore structure model (i.e., the Eu and Zr cations only occupy the 16d and 16c sites, respectively). The obtained refinement profiles for typical compositions of $x = 0.125$ and 0.5 are shown in Figure S1. The results show that ordered structure model overpredicts the intensities of some superlattice reflections for these pyrochlore compositions, further validating their disorder nature.

To highlight the order–disorder transition in the $Eu_2Zr_{2-x}O_{7-2x}$ ($x = 0$–0.5) pyrochlores, the degree of Eu^{3+} cation ordering and the unit cell parameters for these compositions, derived from the PXRD refinements, are shown in Figure 3. The degree of Eu^{3+} cation ordering parameter Φ is defined as $\Phi = 2\sigma - 1$,[64] where σ is the 16d site occupancy of Eu^{3+} cation in the disorder pyrochlore structure.

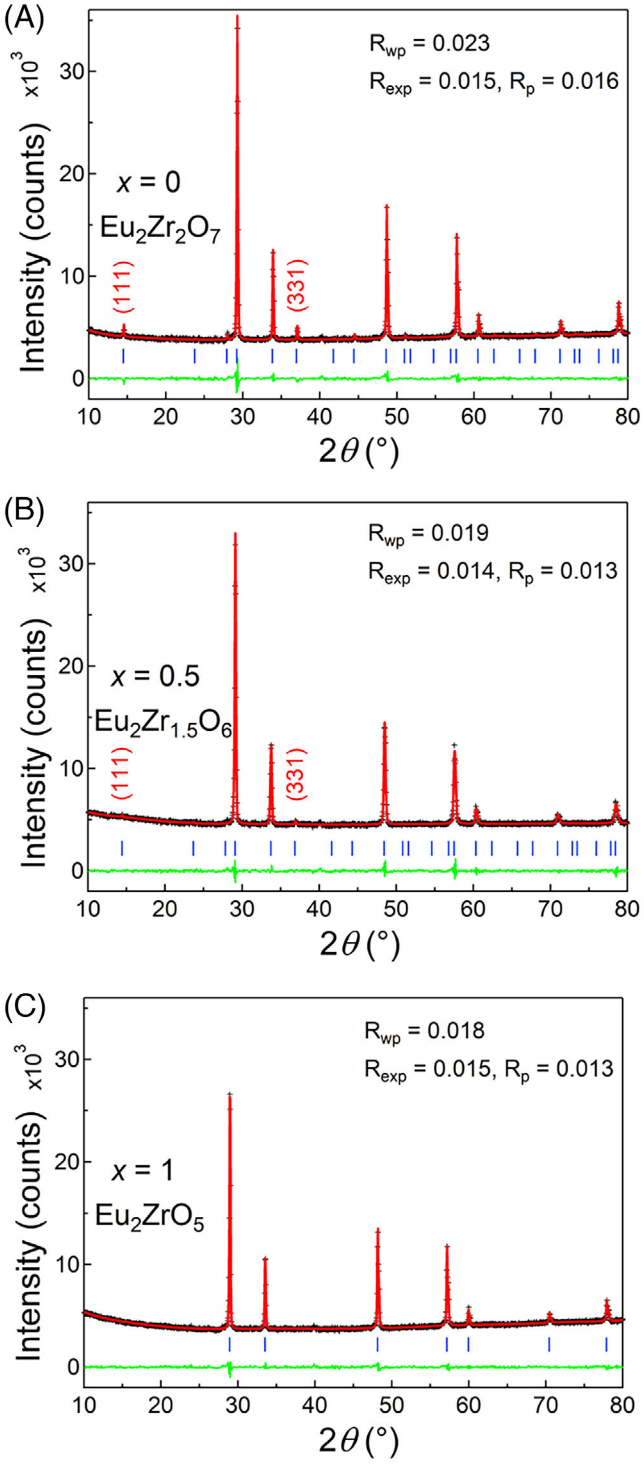

FIGURE 2 Rietveld refinements of PXRD data from typical $Eu_2Zr_{2-x}O_{7-2x}$ solid solutions: (a) $Eu_2Zr_2O_7$ ($x = 0$) with ordered pyrochlore structure (space group $Fd\bar{3}m$), (b) $Eu_2Zr_{1.5}O_6$ ($x = 0.5$) with disordered pyrochlore structure ($Fd\bar{3}m$), and (c) Eu_2ZrO_5 ($x = 1$) with defect fluorite structure ($Fm\bar{3}m$). The graph shows the observed data points (represented by + symbols), the fit by the Rietveld refinement method (the red line), and their difference (the green curve). Blue tick marks show the peak positions for the corresponding structures. The fitting quality parameters (R_{wp}, R_{exp}, and R_p) are also indicated.

TABLE 2 Detailed PXRD Rietveld refinement results for the $Eu_2Zr_{2-x}O_{7-2x}$ (a) pyrochlores ($x = 0–0.5$) and (b) the defect fluorites ($x = 0.625–1$).

(a) Pyrochlore compositions					
x	0	0.125	0.25	0.375	0.5
Unit cell parameter a (Å)	10.5890(2)	10.5962(2)	10.6055(2)	10.6230(3)	10.6213(3)
O1 48*f* site x-coordinate parameter	0.3374(16)	0.3433(16)	0.3443(18)	0.360(3)	0.351(3)
Eu1 16*d* site occ.	1 (fixed)	0.817(10)	0.714(12)	0.557(7)	0.551(7)
Zr1 16*d* site occ.	–	0.183(10)	0.286(12)	0.40625 (fixed)	0.375 (fixed)
Eu2 16*c* site occ.	–	0.183(10)	0.286(12)	0.40625 (fixed)	0.449(7)
Zr2 16*c* site occ.	1 (fixed)	0.754(10)	0.589(12)	0.443(7)	0.375 (fixed)
Degree of Eu cation ordering	approximately 100%	63%	43%	11%	10%
R_{wp}	0.023	0.019	0.021	0.023	0.019
R_{exp}	0.015	0.015	0.015	0.014	0.014
R_p	0.016	0.014	0.015	0.015	0.013

(b) Defect fluorite compositions				
x	0.625	0.75	0.875	1
Unit cell parameter a (Å)	5.3226(1)	5.3300(0)	5.3358(1)	5.3423(1)
R_{wp}	0.019	0.019	0.021	0.018
R_{exp}	0.014	0.016	0.016	0.015
R_p	0.014	0.014	0.016	0.013

Note: The O anion sites 48*f* and 8*b* for all the pyrochlores and the mixed site occupancy parameters for Zr cations, as well as some highly disordered pyrochlores ($x = 0.375$ and 0.5), are constrained to be equally occupied based on the stoichiometries and the order/disorder nature of these solid solutions.

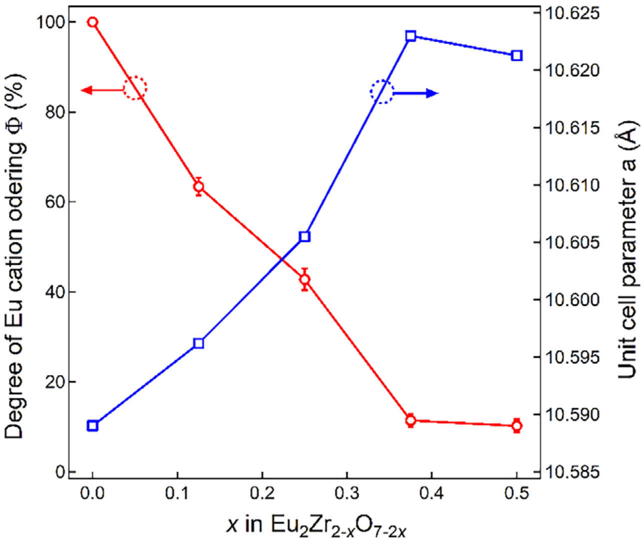

FIGURE 3 Degree of Eu^{3+} cation ordering and unit cell parameters for the $Eu_2Zr_{2-x}O_{7-2x}$ pyrochlores ($x = 0–0.5$), determined from PXRD Rietveld refinements.

Such parameter allows the quantitative characterization of the disordering transition. It is found that Φ parameter decreases to approximately 63% for the $x = 0.125$ composition, and further to approximately 43% for $x = 0.25$, and stabilizes at approximately 10% for $x = 0.375$ and 0.5 compositions. In contrast, the unit cell parameters a for the $Eu_2Zr_{2-x}O_{7-2x}$ ($x = 0–0.5$) pyrochlores are shown to first increase from $a = 10.5890(2)$ Å for $x = 0$ to $a = 10.6230(3)$ Å for $x = 0.375$, then slightly decrease to $a = 10.6213(3)$ Å for $x = 0.5$. Additionally, consistent with previous findings,[65] the O1 48*f* site x-coordinate parameter x(O) is approximately 0.33 for the ordered $Eu_2Zr_2O_7$ pyrochlore, and x(O) parameter slightly increases to the range of approximately 0.34 to approximately 0.36 for the disordered pyrochlores (see Table 2). Based on the PXRD Rietveld refinements, the overall phase transitions in the series are illustrated in Figure 4. It highlights that the observed order–disorder phase transitions are characterized by the increased mixed occupancy of Eu/Zr cation sites (16*c* and 16*d*) in the long-range structures.

3.2 | Diffuse reflectance spectroscopy

Diffuse reflectance spectroscopy has been widely used to investigate actinide valences in nuclear materials.[66] Taken uranium as an example, single-ion absorption bands from U(IV) ion in a $5f^2$ configuration were expected right over the range of visible (vis)/near-infrared (NIR) regions, and those from U(V) ion in a $5f^1$ configuration were mainly located in the near-infrared range,[66] while strong absorption bands in UV region due to the charge transfer were

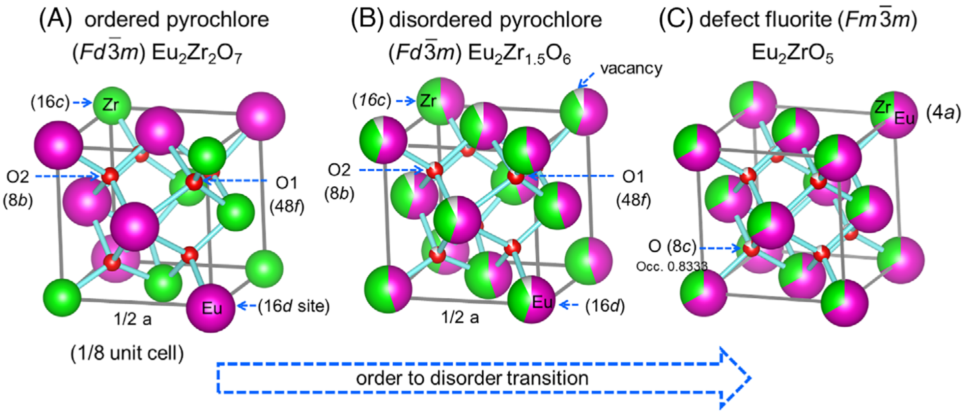

FIGURE 4 The crystal structure transition from (a) ordered pyrochlore $Eu_2Zr_2O_7$, to (b) highly disordered pyrochlore $Eu_2Zr_{1.5}O_6$, then (c) defect fluorite Eu_2ZrO_5.

expected for the U(VI) ion as it lacks the 5f electron. In addition, the absorption bands also shift and/or splitting due to crystal field and spin coupling.[67] These absorption spectral features (band locations and shifts) would help with the determination of U valences and the coordination environment. It is of interest to see whether DRS would be able to provide any characteristic features for the Eu(III) ion in different structure types. Based on theoretical calculations,[68] the characteristic absorption bands in the UV–vis range for Eu(III) ion contain: (i) $^7F_0 \rightarrow {}^5L_6$ (390–405 nm) as the most intense transition in UV–vis region; (ii) $^7F_0 \rightarrow {}^5L_2$ (460–470 nm); (iii) $^7F_0 \rightarrow {}^5L_1$ (520–530 nm); and (iv) $^7F_0 \rightarrow {}^5L_0$ (585–600 nm). DRS spectra of $Eu_2Zr_{2-x}O_{7-2x}$ ($x = 0$–1) solid solutions are shown in Figure 5. The four characteristic absorption bands in order of high to low intensity are: $^7F_0 \rightarrow {}^5L_6$ at 395 nm, $^7F_0 \rightarrow {}^5L_2$ at 470 nm, $^7F_0 \rightarrow {}^5L_1$ at 530 nm, and $^7F_0 \rightarrow {}^5L_0$ at 590 nm. These absorption bands remain un-shifted across the solid solution series. Likewise, the spectra in the NIR region show similar features with multiple absorption bands in the spectral range of 1300–1600 nm. Again, no obvious band shift or splitting is evident corresponding to the phase transitions.

3.3 | Raman spectroscopy

Because x-ray diffraction is more powerful to detect the heavy elements, it is more sensitive to monitor the order–disorder of the cation sub-lattice, thus provides the information of the average crystal structures. On the other hand, Raman spectroscopy is particularly sensitive to metal–oxygen vibrational modes, thus ideal for probing the anion sub-lattice environment. As such, it has been extensively used to investigate the structure transitions and distortions.[69–74]

The basic cell of $A_2B_2O_7$ pyrochlore can be presented as an assembly of BO_6 octahedra linked by A_2O' chains. The structure is constructed by two different types of chemical bonds. While the A–O bonds are much weaker and show ionic character, the B–O bonds are more rigid, slightly less ionic and ensure the cohesion of the structure.[75] These B–O bonds are sensitive to very small changes in either chemical or structural environment, thus evident in Raman spectra. The A and B cations do not contribute to the Raman vibrations, as they are located on the inversion center. The theoretical analyses and selection rules predict six Raman active modes $A_{1g} + E_g + 4F_{2g}$ for the pyrochlore structure with space group $Fd\bar{3}m$.[72–77] Short-range force field calculation[75] predicts that the main contribution to the A_{1g} mode originates from force constants related to O–B–O bending. The E_g mode is generally associated with the combination of the O–B–O bending and the B–O stretching vibrations. Three F_{2g} modes mainly represent a mixture of B–O bond stretching and bending vibrations, while the fourth F_{2g} mode is predominantly due to O–A–O′ bending vibrations.

Figure 6 shows the Raman spectra of the $Eu_2Zr_{2-x}O_{7-2x}$ ($x = 0$–1) solid solution series, using the excitation laser at either 532 or 785 nm. Four distinguished Raman peaks are observed for $Eu_2Zr_2O_7$ pyrochlore, located at approximately 525 cm^{-1} (A_{1g}), and approximately 590, approximately 381, and approximately 307 cm^{-1} (F_{2g}). The E_g mode expected at approximately 338 cm^{-1} is sheltered under the intense and broad F_{2g} mode at approximately 307 cm^{-1}, while another F_{2g} mode calculated at approximately 480 cm^{-1} could be suppressed by 525 cm^{-1} A_{1g} mode or possibly indistinguishable from the background. The A_{1g}, E_g and three F_{2g} modes are usually assigned to the vibration of the ZrO_6 octahedra, while the fourth F_{2g} mode is due to the O–Eu–O′ vibrations.[76,77] The detailed Raman active phonon modes for $Eu_2Zr_{2-x}O_{7-2x}$ ($x = 0$–1)

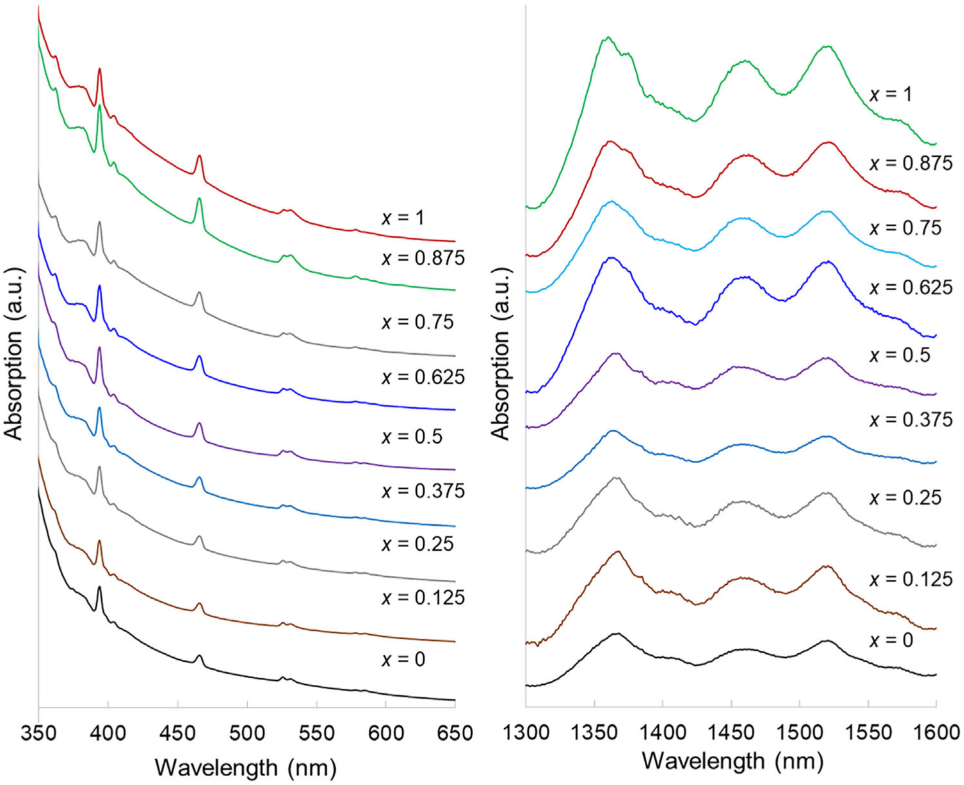

FIGURE 5 Diffuse reflectance spectra (left: UV–vis range; right: NIR range) of $Eu_2Zr_{2-x}O_{7-2x}$ ($x = 0$–1) solid solutions.

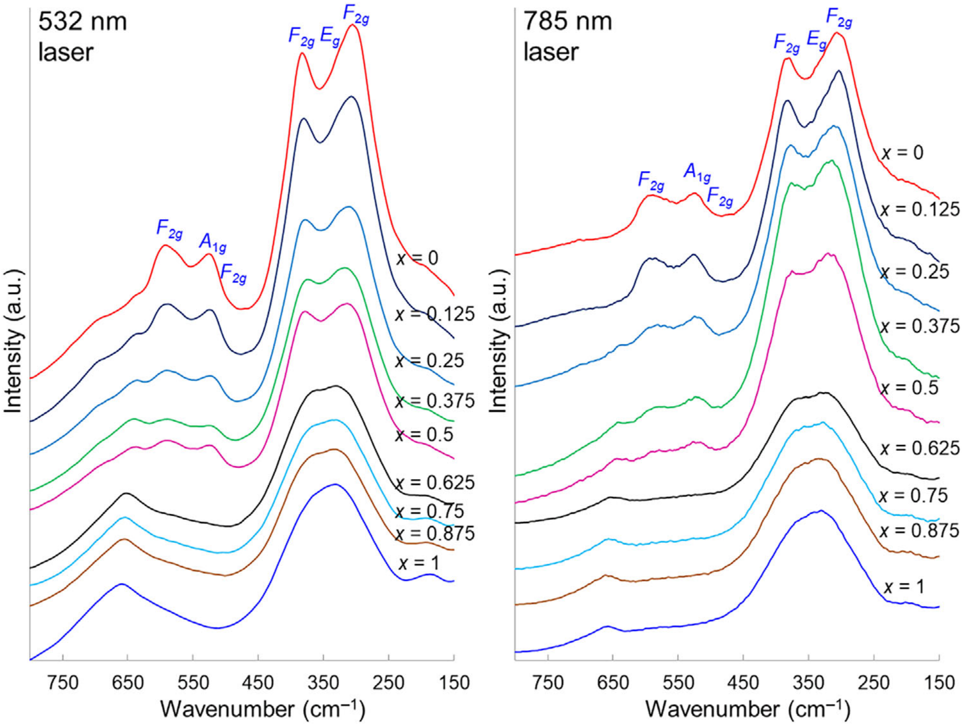

FIGURE 6 Raman spectra of the $Eu_2Zr_{2-x}O_{7-2x}$ ($x = 0$–1) solid solutions, excited by either 532 nm (left) or 785 nm (right) laser.

TABLE 3 Observed Raman active phonon modes for $Eu_2Zr_{2-x}O_{7-2x}$ (x = 0–1, step = 0.125) solid solutions and the simulated Raman frequencies for $Eu_2Zr_2O_7$.

$Eu_2Zr_{2-x}O_{7-2x}$		A_{1g}	E_g	F_{2g} (1)	F_{2g} (2)	F_{2g} (3)	F_{2g} (4)
$x = 0$	Cal. [69]	524	338	598	496	389	298
	Cal. [70]	523	339	581	470	376	288
	Exp. [50]			594		390	295
	Exp. [71]	525		596		380	300
	This work	526/524		592/589		382/380	307/307
$x = 0.125$	This work	524/526		589/585		380/381	308/304
$x = 0.25$		524/526		590/582		379/378	310/306
$x = 0.375$		526/523		589/580		375/376	318/314
$x = 0.5$		526/527		590/579		378/375	314/316
		F_{2g}			C_1 structure		
$x = 0.625$	This work	653/654			338/338		
$x = 0.75$		653/653					
$x = 0.875$		655/653					
$x = 1$		658/659					

Note: Wavenumber A/B: A and B indicate the Raman peaks using 532 and 785 nm laser, respectively.

solid solutions and the simulated Raman frequencies for $Eu_2Zr_2O_7$ are summarized in Table 3.

With gradual decreasing ZrO_2 mol% from x = 0 to x = 1.5, the intensities of the two F_{2g} modes at lower frequencies are hardly changed. But the F_{2g} (3) peaks shift slightly from approximately 381 to approximately 377 cm^{-1} and the F_{2g} (4) peak position increases apparently from approximately 307 to approximately 315 cm^{-1}. Both intensity and position of these two F_{2g} modes are independent of the laser wavelength, which can be clearly observed in Figure 7. In addition, the A_{1g} modes show little variation at approximately 525 cm^{-1} and are independent of the excitation laser energy. However, the peak intensities are reduced significantly from $Eu_2Zr_2O_7$ to $Eu_2Zr_{1.5}O_6$, suggesting the increasing structure disorders associated with oxygen vacancies. Even these materials possess pyrochlore crystal structures, which are confirmed by PXRD data refinements and the characteristic Raman peaks, the structure progressively changes from highly order to disorder along the series. Furthermore, the frequencies of the F_{2g} (1) modes are located at approximately 590 cm^{-1} and do not change with the 532 nm laser, but their positions decrease from 589 to 579 cm^{-1} under 785 nm laser, which is obvious in Figure 8. Similar as A_{1g} mode, these F_{2g} (1) peaks shrink significantly for $Eu_2Zr_{2-x}O_{7-2x}$ materials with $x = 0$ to $x = 1.5$, suggesting high pyrochlore distortion for $Eu_2Zr_{1.5}O_6$ material.

A factor group simulation expects only one Raman mode (F_{2g}) for the fluorite structure with space group $Fm\bar{3}m$.[73] "Cubic"-stabilized zirconia is obtained with lanthanide oxide over certain amount (>0.15 mol%), with the Raman spectrum of the cubic phase exhibiting a broad continuum from approximately 100–800 cm^{-1}.[73] Raman spectra of the solid solution $Eu_2Zr_{2-x}O_{7-2x}$ (x = 0.625–1) shown in Figure 6 exhibit the features of the cubic fluorite structure. All Raman F_{2g} modes are located at the range of 653–659 cm^{-1}, with slight shifting to higher wavenumber at lower ZrO_2 mol%. In addition, the Raman peaks excited by 532 nm laser are more intense than those by 785 nm laser, which are apparent in Figure 8. At the lower energy side, there are broad and strong Raman peaks spreading from 250 to 450 cm^{-1} and centered at approximately 340 cm^{-1} for these four materials.

An early study[73] shows the Raman spectrum of the $Gd_{0.3}Zr_{0.7}O_{1.85}$ compositional material exhibiting cubic fluorite structure with F_{2g} mode centralized at approximately 600 cm^{-1} and another broad Raman peak observed at approximately 310 cm^{-1}. A recent study[43] reports that $Nd_{0.2}Zr_{0.8}O_{1.9}$ and $Nd_{0.3}Zr_{0.7}O_{1.85}$ materials show two broad Raman bands at around 600 and 330 cm^{-1}. The broad band at approximately 600 cm^{-1} is the characteristic of cubic-stabilized zirconia (F_{2g} mode) having defect fluorite structure. Such band is also reported to appear at approximately 610 cm^{-1} for yttria-stabilized zirconia.[78] For stabilized cubic phase of the zirconia, only one Raman active mode and one IR active mode are expected.[79] A major Raman peak is observed at 616 cm^{-1}, which is assigned to the triply degenerate F_{2g} fundamental. This mode arises from the symmetric motions of the oxygen atoms only. Owing to the high symmetry of the tetrahedra, which surround oxygen, this mode arises from the three equivalent motions of oxygen on the three axes, corresponding to symmetric O–Zr–O stretching. For lanthanide-embedded zirconia possessing cubic

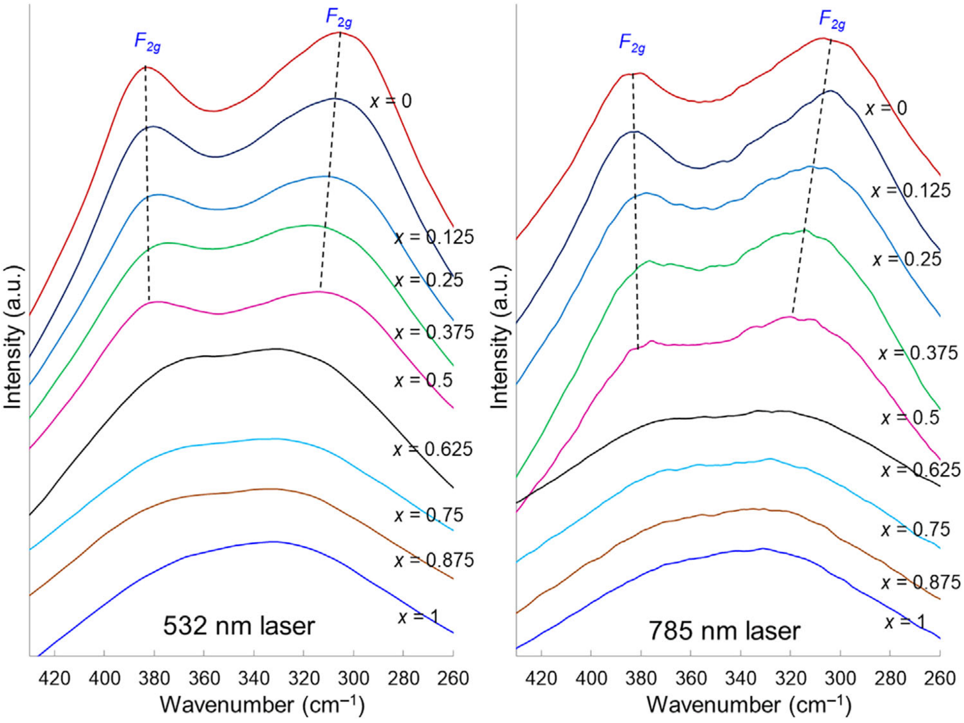

FIGURE 7 Raman spectra of the $Eu_2Zr_{2-x}O_{7-2x}$ ($x = 0$–1) solid solutions, excited by either 532 nm (left) or 785 nm (right) laser in the range of 260–430 cm^{-1}.

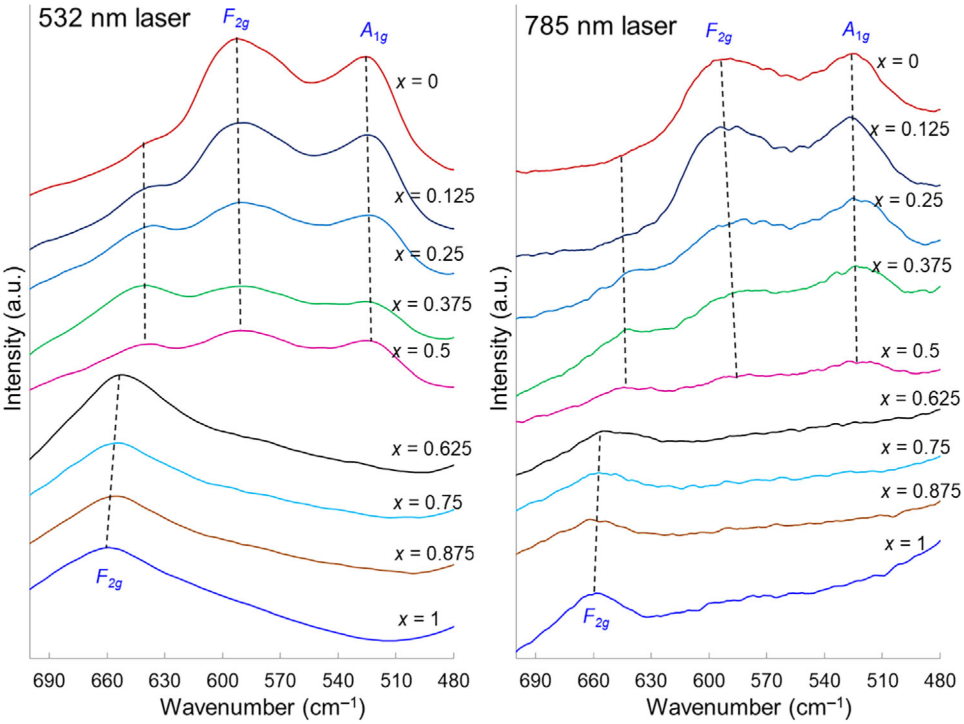

FIGURE 8 Raman spectra of the $Eu_2Zr_{2-x}O_{7-2x}$ ($x = 0$–1) solid solutions, excited by either 532 nm (left) or 785 nm (right) laser in the range of 480–700 cm^{-1}.

fluorite structure, the breadth of the Raman peaks is highly broad and anomalous, suggesting high structural disorder associated with oxygen vacancies, coupled with Zr–O–Zr asymmetric stretching and deformation modes.

In theory, the ordered fluorite structure has only one active Raman mode (T_{2g}), which often appears as a single broad band in the high-frequency region (approximately 600–800 cm^{-1}), due to the presence of nanocrystalline domains of various orientations.[73] With increasing of mol% for Eu, the structure transforms from disordered pyrochlore to defect fluorite. The ordering of the vacancies tends to the same arrangement as in the *C*-type lanthanide sesquioxide structure. The cubic structure with space group *Ia*3 can be described as a fluorite superstructure arising from the ordering of vacancies on the anionic sub-lattice.[73] As a result, the low-frequency broad bands centered at approximately 338 cm^{-1} correspond to vibrations at different degrees of order in the C_1 structure.[73,80] These Raman results may suggest the materials $Eu_2Zr_{2-x}O_{7-2x}$ ($x = 0.625$–1) contain two coherent phases identical in composition: a nanocrystalline defect fluorite-like phase (*F*), and a nanoparticulate ordered fluorite derivative (C_1). Previous study has proposed[80] that the cubic fluorite-derived phases (*F*) ($Fm\bar{3}m$) and C_1 (*Ia*3) have similar lattice parameters in a fluorite setting and the crystal lattices of the nanodomains may be separated by layers of a distorted, nanoparticulate C_1 phase differing in the degree of order.

The results highlight that both PXRD and Raman spectroscopy are essential and complementary for correct phase characterization at bulk and microstructural level, and can provide a better understanding of the phase transitions for materials with various elemental compositions and/or structural disorders.

3.4 | Further discussion

It is generally accepted that the highly ordered-pyrochlore structure ($A_2B_2O_7$) stabilizes in a range of the ionic radius ratio of *A* and *B* site cations (r_A/r_B within 1.46–1.80).[50] For $r_A/r_B < 1.46$, an anion-deficient fluorite structure is expected, whereas a monoclinic layered perovskite structure-type is favored for $r_A/r_B > 1.80$. With the Zr^{4+} or Ti^{4+} cations occupying the *B*-site in six-fold coordination ($r_{\text{Zr4+}} = 0.720$ Å and $r_{\text{Ti4+}} = 0.605$ Å, see Table S1), the formed lanthanide zirconates (*Ln* = La–Gd) and the lanthanide titanates (*Ln* = Sm–Lu) (Ln^{3+} in eight-fold coordination) tend to form pyrochlores. It is experimentally confirmed that decreasing Ln^{3+} radius increases the disorder between the *A*- and *B*-site cations and the tendency to form the fluorite structure.[50] The complete chemical substitution on *A*-site cation induces the structural transition from an ideal ordered-pyrochlore structure to a completely disordered, defect fluorite structure.[81] Alternatively, mixed occupancies of *A*- or *B*-site cations may occur for the pyrochlores.[38,82–84] In these cases, the formation of a pyrochlore or fluorite still depends on the average cation ionic radius ratio of the *A*- and *B*-site cations, under the condition that the discrepancy between ionic radii of the replaced and the original cations is within a tolerant range. The pyrochlore structure is commonly depicted as an ordered derivative of the anion-deficient fluorite structure, so it has a strong tendency to disorder and the compositional modification can cause transitions in the pyrochlore toward a disordered defect-fluorite structure.

In certain circumstances, additional Ln^{3+} cation can occupy the pyrochlore *B*-site. This phenomenon has been observed for a few $Ln_2(Ti_{2-y}Ln_y)O_{7-y/2}$ ($y = 0$–0.67; *Ln* = Tb, Dy, Ho, Er, Tm, Yb, Lu) lanthanide titanate pyrochlores.[85] For the smaller lanthanides (Ho–Lu), a smooth pyrochlore to defect fluorite transition is observed as more Ln^{3+} ions are stuffed into the structure, where the Ln^{3+} and Ti^{4+} ions become completely randomized at the maximum *Ln* composition ($y = 0.67$). Titanate pyrochlores with Tb and Dy constitute ions are rather difficult to stuff, given the larger size discrepancies between the Tb^{3+}/Dy^{3+} (coordination number, CN = 6) and Ti^{4+} ions (Tb^{3+}/Dy^{3+} is approximately 1.51–1.53 times larger than Ti^{4+}). This results in less mixing between the two cations with little disorder on the original Ln^{3+} site. Extra Ln^{3+} cations co-occupy mainly the Ti^{4+} site with disorder mostly on the *B*-site of the pyrochlore structure, but no complete transition to fluorite even at maximum stuffing.

There are several attempts to estimate a tolerance factor and unit cell parameters for pyrochlore oxides.[86–88] The recently proposed empirical formulae listed below are used to define an empirical tolerance factor (Equation 1) and calculate the unit cell parameter (Equation 2),[88] and the calculation results are summarized in Table 4.

$$\tau = 1.43373 - 0.42931\left(\frac{r_A + r_O}{r_B + r_O}\right) \tag{1}$$

$$a = \frac{8}{\sqrt{3}}\left[1.43373\,(r_A + r_O) - 0.42931\frac{(r_A + r_O)^2}{r_B + r_O}\right] \tag{2}$$

where r_A, r_B, and r_O (1.38 Å at CN = 4) are the average ionic radius of the *A*, *B*, and oxygen ions, respectively. These formulas are proposed for compounds with pyrochlore structure based only on the ionic radii of the constituent ions and derived by a statistical treatment of available structural data, and no structural parameters are explicitly used.

As $Eu_2Zr_2O_7$ is close to the transition boundary from the ordered pyrochlore to the defect fluorite (Table S1), the

TABLE 4 The calculation results of the average cation ionic radius ratios ($r_{\mathrm{Eu}}/r_{B(\mathrm{ave})}$), the pyrochlore unit cell parameter (a), and the tolerance factor (τ).

B	$A_2B_{2-x}O_{7-2x}$ or $(A,B)_{4-x}O_{7-2x}$	$r_{B(\mathrm{ave})}$	$r_{\mathrm{Eu}}/r_{B(\mathrm{ave})}$ [a]	a (Å)	Tolerance factor τ	Phase
$x = 0$	$Eu_2Zr_2O_7$	0.720	1.481	10.5484	0.934	ord-pyro.
$x = 0.125$	$Eu_{1.9375}(Zr_{1.875}Eu_{0.0625})O_{6.75}$	0.727	1.466	10.5680	0.935	↓
$x = 0.25$	$Eu_{1.875}(Zr_{1.75}Eu_{0.125})O_{6.5}$	0.735	1.450	10.5888	0.937	
$x = 0.375$	$Eu_{1.8125}(Zr_{1.625}Eu_{0.1875})O_{6.25}$	0.743	1.434	10.6109	0.939	
$x = 0.5$	$Eu_{1.75}(Zr_{1.5}Eu_{0.25})O_6$	0.752	1.417	10.6343	0.941	disor-pyro.
$x = 0.625$	$Eu_{1.6875}(Zr_{1.375}Eu_{0.3125})O_{5.75}$	0.762	1.399	–	–	def-flu.
$x = 0.75$	$Eu_{1.625}(Zr_{1.25}Eu_{0.375})O_{5.5}$	0.772	1.380	–	–	
$x = 0.875$	$Eu_{1.5625}(Zr_{1.125}Eu_{0.4375})O_{5.25}$	0.784	1.360	–	–	
$x = 1.0$	$Eu_{1.5}(ZrEu_{0.5})O_5$	0.796	1.340	–	–	

Abbreviations: def-flu.: defect fluorite; disor-pyro.: disordered-pyrochlore; ord-pyro.: ordered-pyrochlore.

[a] $r_{B(\mathrm{ave})} = [(2-x)r_{\mathrm{Zr}} + xr_{\mathrm{Eu}}/2]/(2-x/2)$.

increment of the average B-site ionic radius would induce a transition to an anion-deficient fluorite structure. The presence of excess of Eu likely leads to an Eu replacement on the Zr site, as the radius of Eu^{3+} (CN = 6) is just 1.315 times larger than Zr^{4+}. With more Eu occupying the Zr site, the average B-site ionic radius increases, leading to the reduction of the average cation ionic radius ratio of the A- and B-site cations (Table 4). As the size of the A-site cation approaches that of the B-site cation, the driving force for structural ordering decreases, and the structure is stable as the defect fluorite structure, $(A,B)_4O_7$. In this case, the disordering of the cation sites as well as the vacancies in the anion sites occur in the structure. This chemically induced, order–disorder pyrochlore, then defect fluorite structural transition is closely associated with the $r_{\mathrm{Eu}}/r_{B(\mathrm{ave})}$ changes.

As shown in Table 4, the calculated pyrochlore cell parameters increase gradually with increasing Ln cations on the B-site from 10.5484 Å ($x = 0$) to 10.6343 Å ($x = 0.5$). These results are in reasonable agreement with the observation in this work, with the cell parameter increasing from 10.5890 to 10.6213 Å for $Eu_2Zr_2O_7$ and $Eu_2Zr_{1.5}O_6$, respectively. This trend is also consistent with the observation for $Ln_2(Ti_{2-y}Ln_y)O_{7-y/2}$ ($y = 0$–0.67) materials[85] in which excess smaller Ln are stuffed on the Ti site, leading to not only the enlargement of the cell parameter, but also the eventual pyrochlore to defect fluorite transition.

The tolerance factor τ (Equation 1) is symmetrically distributed ranging from 0.871 to 0.948 after fitting the histogram with a Gaussian function, corresponding to the r_A/r_B values from approximately 1.80 to approximately 1.38. The tolerance factor is centered at $\tau = 0.913$ in the Gaussian distribution. For pyrochlores with a tolerance factor near this value, the ionic radii ratio r_A/r_B is near 1.6, which is almost in the middle of the r_A/r_B range (1.46–1.80) proposed by Subramanian et al.[50] as the requirement for the formation of pyrochlore structure. The calculated tolerance factors are 0.934 for $Eu_2Zr_2O_7$ and 0.941 for $Eu_2Zr_{1.5}O_6$ (Table 4), corresponding to the r_A/r_B values from 1.481 to 1.417, within the tolerance range for a pyrochlore structure.[88] $Eu_2Zr_{1.5}O_6$ can be termed as $Eu_{1.75}(Zr_{1.5}Eu_{0.25})O_6$ suggesting that 12.5 mol% of Eu is relocated from pyrochlore A-site to B-site, by this re-occupation, the pyrochlore is varied from ordered to disordered structure, which has been confirmed by the long-range XRD analyses and the short-range Raman results. The formation of the pyrochlores outside $1.46 \leq r_A/r_B \leq 1.80$ range but within the tolerance values may suggest the pyrochlore structures are disordered, which is the intrinsic feature of this special crystal structure.

It should be clarified that the formulation of Equations (1) and (2) may not be the general criteria for predicting the formation and stability of the pyrochlore structure. For example, Fuentes et al.[38] have synthesized the mixed A-site pyrochlores, using mixed-oxide route and heat treatment at 1400°C. By applying Equation (1) to the r_A and r_B assuming nominal distributions at the A- and B-sites, all the mixed oxides should have the pyrochlore structure,[38] which is contrary to their experimental results. Their results showed that many of them do not present long-range pyrochlore ordering, while, on the other hand, Raman spectroscopy suggests that most of them are short-range ordered. It is reasonable to believe that these observations lead to two indications. One is that the existing tolerance factor formulation for pyrochlore oxides may be not robust/comprehensive enough to predict the formation of the pyrochlore or fluorite structure. Another is that there may be sufficient nonnegligible amount of the antisite defects present in the structure. The real average r_A/r_B values based on the final composition on the A- and B-sites can be significantly different from the nominal ones, by which all the tolerance factors are used to predict the crystal structure.

3.5 | Implications and perspectives

This work highlights the flexible crystal chemistry of zirconate materials as candidate waste forms for actinide immobilization. The obvious advantages, for example, good chemical durability and excellent radiation tolerance, ensure that zirconates are suitable waste forms for the separated minor actinides[89] and the lanthanide-rich actinide waste stream from the reprocessing of spent nuclear fuel discharged from the light water reactors.[90]

In general, zirconates require high-temperature sintering to become dense ceramics suitable as waste forms. However, hydrothermal synthesis of zirconate nanoparticles is possible and offers an alternative for low-temperature processing of zirconate materials.[91] Some pioneer work to stabilize zirconate nanoparticles in glass matrix as advanced glass–ceramic waste forms provided an alternative processing route, which warrants further research effort.[92]

4 | CONCLUSIONS

A solid solution series of compounds $Eu_2Zr_{2-x}O_{7-2x}$ ($x = 0$–1, step $= 0.125$) have been fabricated using a co-precipitation method and subsequently sintering at 1400°C. The structures of the solid solutions undergo gradual phase transitions from ordered pyrochlore $Eu_2Zr_2O_7$ to highly disordered pyrochlore $Eu_2Zr_{1.5}O_6$, then to defect fluorite Eu_2ZrO_5, which are confirmed by PXRD data with Rietveld structure refinements. DRS provides characteristic absorption bands for Eu^{3+} ions, but shows little distinctive spectral feature to distinguish the structure types. In contrast, Raman spectroscopy with two different wavelength lasers clearly shows the phase transition from pyrochlore to fluorite for the series, highlighting the advantage of micro-Raman for probing local structures.

Overall, lanthanide zirconate materials demonstrate the unique structural flexibility, and are candidate host phases for actinide-rich waste streams especially suitable for conditioning of separated minor actinides.

ACKNOWLEDGMENTS

All materials were synthesized and characterized at the facilities under Nuclear Science and Technology (NST) at ANSTO.

ORCID

Yingjie Zhang https://orcid.org/0000-0001-6321-4696

REFERENCES

1. Liu Z, Yang B, Tian L, Zhang F. Development and outlook of advanced nuclear energy technology. Energy Strategy Rev. 2021;34:100630.
2. Baron P, Cornet SM, Collins ED, DeAngelis G, Del Cul G, Fedorov Y, et al. A review of separation processes proposed for advanced fuel cycles based on technology readiness level assessments. Progr Nucl Energy. 2019;117:103091.
3. Zhang Y, Kong L, Ionescu M, Gregg DJ. Current advances on titanate glass–ceramic composite materials as waste forms for actinide immobilization: a technical review. J Eur Ceram Soc. 2022:42(5):1852–76.
4. Gin S, Abdelouas A, Criscenti LJ, Ebert WL, Ferrand K, Geisler T, et al. An international initiative on long-term behavior of high-level nuclear waste glass. Mater Today. 2013;16(6):243–48.
5. Kochkin B, Malkovsky V, Yudintsev S, Petrov V, Ojovan M. Problems and perspectives of borehole disposal of radioactive waste. Prog Nucl Energy. 2021;139:103867.
6. Dayal P, Farzana R, Zhang Y, Lumpkin G, Holmes R, Triani G, et al. Profiling hot isostatically pressed canister-wasteform interaction for pu bearing zirconolite-rich wasteforms. J Am Ceram Soc. 2022;105(8):5359–72.
7. Zhang Y, Stewart MSW, Li H, Carter ML, Vance ER, Moricca S. Zirconolite-rich titanate ceramics for immobilization of actinides—waste form/HIP can interactions and chemical durability. J Nucl Mater. 2009;395:69–74.
8. Kong L, Karatchevtseva I, Zhang Y, Wei T. The incorporation of Nd or Ce in $CaZrTi_2O_7$ zirconolite: ceramic versus glass–ceramics. J Nucl Mater. 2020;543:152583.
9. Vance ER, Zhang Y, Gregg DJ. Ceramic waste forms. In: Konings R, Stoller R, editors. Comprehensive nuclear materials. 2nd ed. Vol 6. Elsevier; 2020. p. 445–66.
10. Zhang Y, Li H, Moricca S. Pyrochlore-structured titanate ceramics for immobilization of actinides: hot isostatic pressing (HIPing) and stainless steel/waste form interactions. J Nucl Mater. 2008;377:470–75.
11. Kong L, Karatchevtseva I, Aughterson RD, Davis J, Zhang Y, Lumpkin GR, et al. New pathway for the preparation of pyrochlore $Nd_2Zr_2O_7$ nanoparticles and densification of bulk ceramic. Ceram Int. 2015;41(6):7618–25.
12. Zhang Y, Mir AH. A review of brannerite structured materials for nuclear waste management. J Nucl Mater. 2023;583:154512.
13. Zhang Y, Lumpkin GR, Li H, Blackford MG, Colella M, Carter ML, et al. Recrystallization of amorphous natural brannerite through annealing: The effect of radiation damage on the chemical durability of brannerite. J Nucl Mater. 2006;350:293–300.
14. Zhang Y, Wei T, Zhang Z, Kong L, Dayal P, Gregg DJ. Uranium brannerite with Tb(III)/Dy(III) ions: phase formation, structures, and crystallizations in glass. J Am Ceram Soc. 2019;102(12):7699–709.
15. Rafiuddin MR, Donato G, McCaugherty S, Mesbah A, Grosvenor AP. Review of rare-earth phosphate materials for nuclear waste sequestration applications. ACS Omega. 2022;7(44):39482–90.
16. Clavier N, Podor R, Dacheux N. Crystal chemistry of the monazite structure. J Eur Ceram Soc. 2011;31(6):941–76.
17. Orlova AI. Isomorphism in d-and f-element phosphates having framework crystal structure and crystallochemical conception of NZP matrix for radionuclide immobilisation. Czechoslovak J Phys. 2003;53:A649–55.
18. Kong L, Karatchevtseva I, Chironi I, Wei T, Zhang Y. $CaZrTi_2O_7$ zirconolite synthesis: from ceramic to glass–ceramic. Int J Appl Ceram Technol. 2019;16(4):1460–70.
19. Zhang Y, Gregg DJ, Kong L, Jovanovich M, Triani G. Zirconolite glass–ceramics for plutonium immobilization: the effects

of processing redox conditions on charge compensation and durability. J Nucl Mater. 2017;490:238–41.

20. Zhang Y, Zhang Z, Thorogood G, Vance ER. Pyrochlore based glass–ceramics for the immobilization of actinide-rich nuclear wastes: from concept to reality. J Nucl Mater. 2013;432:545–47.
21. Kong L, Karatchevtseva I, Zhang Y. A new method for production of glass–$Ln_2Ti_2O_7$ pyrochlore (Ln = Gd, Tb, Er, Yb). J Eur Ceram Soc. 2017;37(15):4963–72.
22. Zhang Y, Kong L, Karatchevtseva I, Aughterson RD, Gregg DJ, Triani G. Development of brannerite glass–ceramics for the immobilization of actinide-rich radioactive wastes. J Am Ceram Soc. 2017;100(9):4341–51.
23. Zhang Y, Karatchevtseva I, Kong L, Wei T, Zhang Z. Structural and spectroscopic studies on the crystallization of uranium brannerite phases in glass. J Am Ceram Soc. 2018;101:5219–28.
24. Scales N, Dayal P, Aughterson RD, Zhang Y, Gregg DJ. Sodium zirconium phosphate based glass–ceramic composites as potential waste forms for the immobilization of nuclear wastes. J Am Ceram Soc. 2022;105:901–12.
25. Li L, Wang F, Liao Q, Wang Y, Zhu H, Zhu Y. Synthesis of phosphate based glass–ceramic waste forms by a melt-quenching process: the formation process. J Nucl Mater. 2020;528:151854.
26. Lumpkin GR, Aughterson RD. Perspectives on pyrochlores, defect fluorites, and related compounds: building blocks for chemical diversity and functionality. Front Chem. 2021;9:778140.
27. Liu Z, Wang L, Ding C, Tang M, Xie H, Li T, et al. Structural evolution and chemical durability of uranium-doped high-entropy pyrochlore. Ceram Int. 2024;50:5955–61.
28. Sun J, Zhou J, Li L, Hu Z, Chan T-S, Vitova T, et al. Atomic controllable anchoring of uranium into zirconate pyrochlore with ultrahigh loading capacity. Chem Commun. 2022;58:3469–72.
29. Tang Z, Huang Z, Han W, Qi J, Shi Y, Ma N, et al. Uranium-incorporated pyrochlore $La_2(U_xMg_xZr_{1-2x})_2O_7$ nuclear waste form: structure and phase stability. Inorg Chem. 2020;59:9919–26.
30. Malachevsky MT, Rodríguez Salvador D, Leiva S, D'Ovidio CA. Cubic phases in the Gd_2O_3-ZrO_2 and Dy_2O_3-TiO_2 systems for nuclear industry applications. J Ceram. 2015;2015:298690.
31. Gregg DJ, Zhang Z, Thorogood GJ, Kennedy BJ, Kimpton JA, Griffiths GJ, et al. Cation antisite disorder in uranium-doped gadolinium zirconate pyrochlores. J Nucl Mater. 2014;452:474–78.
32. Zhang FX, Lang M, Tracy C, Ewing RC, Gregg DJ, Lumpkin GR. Incorporation of uranium in pyrochlore oxides and pressure-induced phase transitions. J Solid State Chem. 2014;219:49–54.
33. Gregg DJ, Zhang Y, Zhang Z, Karatchevtseva I, Blackford MG, Triani G, et al. Crystal chemistry and structures of uranium-doped gadolinium zirconates. J Nucl Mater. 2013;438:144–53.
34. Gregg DJ, Zhang Y, Middleburgh SC, Conradson SD, Triani G, Lumpkin GR, et al. The incorporation of plutonium in lanthanum zirconate pyrochlore. J Nucl Mater. 2013;443:444–51.
35. Martin PM, Belin RC, Valenza PJ, Scheinost AC. EXAFS study of the structural phase transition in the americium zirconate pyrochlore. J Nucl Mater. 2009;385:126–30.
36. Nästren C, Jardin R, Somers J, Walter M, Brendebach B. Actinide incorporation in a zirconia based pyrochlore $(Nd_{1.8}An_{0.2})Zr_2O_{7+x}$ (An = Th, U, Np, Pu, Am). J Solid State Chem. 2009;182:1–7. doi: 10.1016/j.jssc.2008.09.017
37. Wang Y, Jing C, Ding Z-Y, Zhang Y-Z, Wei T, Ouyang J-H, et al. The structure, property, and ion irradiation effects of pyrochlores: a comprehensive review. Crystals. 2023;13:143.
38. Fuentes AF, Montemayor SM, Maczka M, Lang M, Ewing RC, Amador U. A critical review of existing criteria for the prediction of pyrochlore formation and stability. Inorg Chem. 2018;57:12093–105.
39. Popov VV, Menushenkov AP, Gaynanov BR, Zubavichus YV, Svetogorov RD, Yastrebtsev AA, et al. Features of formation and evolution of crystal and local structures in nanocrystalline $Ln_2Zr_2O_7$ (A = La-Tb). J Phys Conf Ser. 2017;941:012079.
40. Brik MG, Srivastava AM. Pyrochlore structural chemistry: predicting the lattice constant by the ionic radii and electronegativities of the constituting ions. J Am Ceram Soc. 2012;95:1454–60.
41. Shlyakhtina AV, Shcherbakova LG. New solid electrolytes of the pyrochlore family. Russ J Electrochem. 2012;48:1–25. doi: 10.1134/S1023193512010144
42. Aughterson R, Lumpkin G, Zhang Z, Avdeev M, Kong L. Crystal chemistry and ion-irradiation resistance of Ln_2ZrO_5 compounds with Ln = Sm, Eu, Gd and Tb. J Am Ceram Soc. 2022;105:3521–33.
43. Nandi C, Jain D, Grover V, Krishnan K, Banerjee J, Prakash A, et al. ZrO_2-$NdO_{1.5}$ system: investigations of phase relation and thermophysical properties. Mater Design. 2017;121:101–8.
44. Popov VV, Menushenkov AP, Zubavichus YV, Yaroslavtsev AA, Leshchev DS, Kulik ES, et al. Specific features of the crystal and local structures of compounds formed in the Dy_2O_3–HfO_2 system. Russ J Inorg Chem. 2016;61:1135–43.
45. Shlyakhtina AV, Abrantes JCC, Gomes E, Shchegolikhin AN, Vorobieva GA, Maslakov KI, et al. Effect of Pr^{3+}/Pr^{4+} ratio on the oxygen ion transport and thermomechanical properties of the pyrochlore and fluorite phases in the ZrO_2–Pr_2O_3 system. Int J Hydrogen Energy. 2016;41:9982–92.
46. Popov VV, Menushenkov AP, Zubavichus YV, Korovin SA, Fortal'nova EA, Kruglov AB, et al. Structural characteristics and thermophysical properties of complex ceramic oxides in the system Dy_2O_3–HfO_2. Glass Ceram. 2016;73:47–52.
47. Belov DA, Shlyakhtina AV, Abrantes JCC, Chernyak SA, Gasymova GA, Karyagina OK, et al. Electrochemical behavior of the pyrochlore- and fluorite-like solid solutions in the Pr_2O_3–ZrO_2 system. Part I. Solid State Ionics. 2015;271:79–85.
48. Shlyakhtina AV, Kolbanev IV, Knotko AV, Boguslavskii MV, Stefanovich SY, Karyagina OK, et al. Ionic conductivity of $Ln_{2+x}Zr_{2-x}O_{7-x/2}$ (Ln = Sm–Gd) solid solutions. Inorg Mater. 2005;41:854–63.
49. Zinkevich M, Wang C, Morales FM, Rühle M, Aldinger F. Phase equilibria in the ZrO_2–$GdO_{1.5}$ system at 1400–1700°C. J Alloys Compd. 2005;398:261–68.
50. Subramanian MA, Aravamudan G, Subba GV. Oxide pyrochlores—a review. Prog Solid State Chem. 1983;15:55–143.
51. Withers RL, Thompson JG, Barlow PJ. An electron, and x-ray powder, diffraction study of cubic, fluorite-related phases in various ZrO_2–Ln_2O_3 systems. J Solid State Chem. 1991;94:89–105.
52. Tabira Y, Withers RL, Barry JC, Elcoro L. The strain-driven pyrochlore to "defect fluorite" phase transition in rare earth sesquioxide stabilized cubic zirconias. J Solid State Chem. 2001;159:121–29.
53. Jucha S, Grzegorz M, Mikuśkiewicz M. Synthesis and characterization of thermal properties of type Eu_2O_3-ZrO_2 sinters. Arch Metall Mater. 2016;61:1121–28.
54. Fabrichnaya O, Kriegel MJ, Pavlyuchkov D, Seidel J, Dzuban A, Savinykh G, et al. Heat capacity for the $Eu_2Zr_2O_7$ and phase

relations in the ZrO_2–Eu_2O_3 system: experimental studies and calculations. Thermochim Acta. 2013;558:74–82.

55. Lang M, Zhang F, Zhang J, Wang J, Lian J, Weber WJ, et al. Review of $A_2B_2O_7$ pyrochlore response to irradiation and pressure. Nucl Instrum Methods Phys Res B. 2010;268:2951–59.
56. Zhang J, Zhang F, Lang M, Lu F, Lian J, Ewing RC. Ion-irradiation-induced structural transitions in orthorhombic Ln_2TiO_5. Acta Mater. 2013;61:4191–99.
57. Aughterson RD, Zaluzec NJ, Lumpkin GR. Synthesis and ion-irradiation tolerance of the Dy_2TiO_5 polymorphs. Acta Mater. 2021;204:116518.
58. Whittle KR, Blackford MG, Aughterson RD, Lumpkin GR, Zaluzec NJ. Ion irradiation of novel yttrium/ytterbium-based pyrochlores: the effect of disorder. Acta Mater. 2011;59:7530–37.
59. Hiroshi Y, Hanako N, Katsuyoshi K, Katsuhiro N. Electrical conductivity anomaly around fluorite–pyrochlore phase boundary. Solid State Ionics. 2003;158:359–65.
60. Shlyakhtina AV, Shcherbakova LG. Polymorphism and high-temperature conductivity of $Ln_2M_2O_7$ (Ln = Sm—Lu; M = Ti, Zr, Hf) pyrochlores. Solid State Ionics. 2011;192:200–204.
61. Coelho A. TOPAS-Academic V5. Brisbane: Coelho Software; 2012.
62. Hagiwara T, Nomura K, Kageyama H. Differences in local structures around zirconium atoms in $Eu_2Zr_2O_7$ and $La_2Zr_2O_7$. Solid State Ionics. 2019;335:32–37.
63. Joergensen, CK, Rittershaus, E. Powder-diagram and spectroscopic studies of mixed oxides of lanthanides and quadrivalent metal. Kgl Dan Vidensk Selsk Mat-Fys Medd. 1967;35(15):37.
64. Zhang FX, Lang M, Ewing RC. Atomic disorder in $Gd_2Zr_2O_7$ pyrochlore. App Phys Lett. 2015;106:191902.
65. Moun S, Yadav CS. Structure and magnetic studies of geometrically frustrated disordered pyrochlores $A_2Zr_2O_7$: (A = Eu, Gd, Er). J Magn Magn Mater. 2022;553:169255.
66. Vance ER, Zhang Y, Zhang Z, Gregg DJ, McLeod T, Jovanovic M. Solid solutions of higher valence states of actinides in TiO_2 and ZrO_2-Y_2O_3. J Nucl Mater. 2015;462:268–72.
67. Vance ER, Zhang Y, Zhang Z. Diffuse reflectance and x-ray photoelectron spectroscopy of uranium in ZrO_2 and $Y_2Ti_2O_7$. J Nucl Mater. 2010;400:8–14.
68. Zhang Y, Vance ER, Finnie KS, Begg BD, Carter ML. Uranium ion valences in perovskite, zirconolite and pyrochlore from near infrared diffuse reflectance spectroscopy, In: Alvarez R, Bryan ND, May I, editors. Recent advances in actinide sciences. London, UK: The Royal Society of Chemistry; 2006. p. 343.
69. Binnemans K. Interpretation of europium(III) spectra. Coord Chem Rev. 2015;295:1–45. doi: 10.1016/j.ccr.2015.02.015
70. Kushwaha AK, Mishra SP, Vishwakarma MK, Chauhan S, Jappor HR, Khenata R, et al. Theoretical study of thermal conductivity, mechanical, vibrational and thermodynamical properties of $Ln_2Zr_2O_7$ (Ln = La, Nd, Sm, and Eu) pyrochlore. Inorg Chem Commun. 2021;127:108495.
71. Nandi S, Jana YM, Gupta HC. Lattice dynamical investigation of the Raman and infrared wave numbers and heat capacity properties of the pyrochlores $R_2Zr_2O_7$ (R = La, Nd, Sm, Eu). Phys Chem Solids. 2018;115:347–54.
72. Maram PS, Ushakov SV, Weber RJK, Benmore CJ, Navrotsky A. In situ diffraction from levitated solids under extreme conditions—structure and thermal expansion in the Eu_2O_3–ZrO_2 system. J Am Ceram Soc. 2015;98:1292–99.
73. Scheetz BE, White WB. Characterization of anion disorder in zirconate $A_2B_2O_7$ compounds by Raman spectroscopy. J Am Ceram Soc. 1979;62:468–70.
74. Michel D, Jorba MPY, Collongues R. Study by Raman spectroscopy of order–disorder phenomena occurring in some binary oxides with fluorite-related structures. J Raman Spectrosc. 1976;5:163–80.
75. Vandenborre MT, Husson E, Chatry JP, Michel D. Rare-earth titanates and stannates of pyrochlore structure; vibrational spectra and force fields. J Raman Spectrosc. 1983;14:63–71.
76. Brown S, Gupta HC, Alonso JA, Martinez-Lope MJ. Vibrational spectra and force field calculation of $A_2Mn_2O_7$ (A = Y, Dy, Er, Yb) pyrochlores. J Raman Spectrosc. 2003;34:240–43.
77. Kong L, Karatchevtseva I, Gregg DJ, Blackford MG, Holmes R, Triani G. $Gd_2Zr_2O_7$ and $Nd_2Zr_2O_7$ pyrochlore prepared by aqueous chemical synthesis. J Eur Ceram Soc. 2013;33:3273–85.
78. Kong L, Karatchevtseva I, Gregg DJ, Blackford MG, Holmes R, Triani G. A novel chemical route to prepare pyrochlore $La_2Zr_2O_7$. J Am Ceram Soc. 2013;96:935–41.
79. Semjonow AJ, Anastassakis E. Asymmetry of defect-induced Raman spectra in yttria-stabilized zirconia. Physica A. 1993;201:416–20.
80. López EF, Escribano VS, Panizza M, Carnasciali MM, Busca G. Vibrational and electronic spectroscopic properties of zirconia powders. J Mater Chem. 2001;11:1891–97.
81. Ewing RC, Weber WJ, Lian J. Nuclear waste disposal—pyrochlore ($A_2B_2O_7$): nuclear waste form for the immobilization of plutonium and "minor" actinides. J Appl Phys. 2004;95:5949–71.
82. Pilania G, Puchala B, Uberuaga BP. Distortion-stabilized ordered structures in $A_2BB'O_7$ mixed pyrochlores. NPJ Comput Mater. 2019;5:7.
83. Teng Z, Tan Y, Zeng S, Meng Y, Chen C, Han X, et al. Preparation and phase evolution of high-entropy oxides $A_2B_2O_7$ with multiple elements at A and B sites. J Eur Ceram Soc. 2021;41:3614–20.
84. Marlton FP, Zhang Z, Zhang Y, Proffen TE, Ling CD, Kennedy BJ. Lattice disorder and oxygen migration pathways in pyrochlore and defect-fluorite oxides. Chem Mater. 2021;33:1407–15.
85. Lau GC, Muegge BD, McQueen TM, Duncan EL, Cava RJ. Stuffed rare earth pyrochlore solid solutions. J Solid State Chem. 2006;179:3126–35.
86. Chakoumakos BC. Systematics of the pyrochlore structure type, ideal $A_2B_2X_6Y$. J Solid State Chem. 1984;53:120–29.
87. Cai L, Arias AL, Nino JC. The tolerance factors of the pyrochlore crystal structure. J Mater Chem. 2011;21:3611–18.
88. Mouta R, Silva RX, Paschoal CWA. Tolerance factor for pyrochlores and related structures. Acta Crystallogr B Struct Sci Cryst Eng Mater. 2013;69:439–45.
89. Gelis AV, Kozak P, Breshears AT, Brown MA, Launiere C, Campbell EL, et al. Closing the nuclear fuel cycle with a simplified minor actinide lanthanide separation process (ALSEP) and additive manufacturing. Sci Rep. 2019;9:12842.
90. Stefanovsky SV, Yudintsev SV, Shiryaev AA, Murzin VY, Trigub AL. Phase partitioning and uranium speciation in brannerite based ceramics. J Eur Ceram Soc. 2017;37:771–77.
91. Sun J, Zhou J, Hu Z, Chan T-S, Liu R, Yu H, et al. Controllable sites and high-capacity immobilization of uranium in $Nd_2Zr_2O_7$ pyrochlore. J Synchrotron Radiat. 2022;29(1):37–44.

92. Boccaccini AR, Atiq S, Grimes RW. Hot-pressed glass matrix composites containing pyrochlore phase particles for nuclear waste encapsulation. Adv Eng Mater. 2003;5(7):501–8.

SUPPORTING INFORMATION

Additional supporting information can be found online in the Supporting Information section at the end of this article.

How to cite this article: Kong L, Wang Z, Karatchevtseva I, Zhang Y. Phase transition in $Eu_2Zr_{2-x}O_{7-2x}$ ($x = 0$–1) solid solutions: A combined structural and spectroscopic study. J Am Ceram Soc. 2024;107:7604–18.
https://doi.org/10.1111/jace.20031